

Infrared Space Observatory Polarimetric Imaging of the Egg Nebula (RAFGL 2688)¹

Joel H. Kastner², Jingqiang Li², Ralf Siebenmorgen³ and David A. Weintraub⁴

Received _____; accepted _____

ABSTRACT

We present polarimetric imaging of the protoplanetary nebula RAFGL 2688 obtained at $4.5 \mu\text{m}$ with the Infrared Space Observatory (ISO). We have deconvolved the images to remove the signature of the point spread function of the ISO telescope, to the extent possible. The deconvolved $4.5 \mu\text{m}$ image and polarimetric map reveal a bright point source with faint, surrounding reflection nebulosity. The reflection nebula is brightest to the north-northeast, in agreement with previous ground- and space-based infrared imaging. Comparison with previous near-infrared polarimetric imaging suggests that the polarization of starlight induced by the dust grains in RAFGL 2688 is more or less independent of wavelength between $2 \mu\text{m}$ and $4.5 \mu\text{m}$. This, in turn, indicates that scattering dominates over thermal emission at wavelengths as long as $\sim 5 \mu\text{m}$, and that the dust grains have characteristic radii $< 1 \mu\text{m}$.

Subject headings: stars: mass loss — protoplanetary nebulae: individual (AFGL 2688) — dust — polarization

¹Based on observations with ISO (Kessler et al. 1996), an ESA project with instruments funded by ESA Member States (especially the PI countries: France, Germany, the Netherlands and the United Kingdom) with the participation of ISAS and NASA.

²Chester F. Carlson Center for Imaging Science, Rochester Institute of Technology, 54 Lomb Memorial Dr., Rochester, NY 14623

³European Southern Observatory, Karl-Schwarzschildstr. 2, 85748 Garching b. Munich, Germany

⁴Dept. of Physics and Astronomy, Vanderbilt University, Nashville, TN, 37235, U.S.A.

1. Introduction

Stellar mass loss during post-main sequence stellar evolution is, more often than not, an axisymmetric, rather than spherically symmetric, process. However, a coherent explanation for the transformation from quasi-spherical red giant to bipolar planetary nebula remains elusive. During pre-main sequence evolution, bipolar outflow is evidently an inevitable consequence of the presence of a circumstellar, protoplanetary disk. But — neglecting the possibility that some evolved stars may retain massive, long-lived, “fossil” protoplanetary disks (Kastner & Weintraub 1995) — there is no obvious natural “collimating agent” during post-main sequence stellar evolution. Hence the shaping of bipolar planetary nebulae (PNs), the endpoints of stellar evolution for intermediate-mass ($1-8 M_{\odot}$) stars, is a topic of considerable contemporary interest in astronomy (see reviews in Kastner, Soker, & Rappaport 2000a).

The object RAFGL 2688 (The Egg Nebula) has long been regarded as prototypical of the class of evolved bipolar nebulae. The nebula was first identified as a bright far-IR source associated with axisymmetric optical nebulosity by Ney et al. (1975). Based on its radio molecular emission line profiles, Zuckerman et al. (1976) proposed that the object was representative of the rapid transition from red giant to planetary nebula. Immediately following its discovery, RAFGL 2688 was established as a source of highly polarized optical and near-IR emission (e.g., Jones & Dyck 1978). The large net polarization in these early, large aperture measurements was thought to originate with the scattering of starlight by circumstellar dust, where the dust grain population is distributed in axisymmetric fashion about the central star. The latitudinal dependence of the dust density results in large opacities along the equatorial plane but relatively small opacities toward higher latitudes. Assuming the polar axis is nearly in the plane of the sky, the star itself would then be obscured along our line of sight, whereas starlight can still escape along polar (but not

equatorial) directions and be scattered toward Earth.

This qualitative model of the structure of RAFGL 2688 has since been confirmed, first by Monte Carlo scattering models (Yusef-Zadeh et al. 1984) and, most recently, by high spatial resolution Hubble Space Telescope near-infrared polarimetric imaging observations (Sahai et al. 1998a; Fig. 1). The HST imaging demonstrates conclusively that the nebula displays the centrosymmetric patterns and large degree of linear polarization expected for an axisymmetric distribution of dust grains illuminated by a central source. Furthermore, the HST observations have established the position of the central illuminator, relative to the extended nebulosity, to within ~ 100 AU (Weintraub et al. 2000). In addition to the unseen illuminator, RAFGL 2688 contains a prominent, central source of direct (unpolarized) emission that is only detectable at wavelengths $> 1.5\mu\text{m}$ (Sahai et al. 1998a; Weintraub et al. 2000). The relationship of this source to the illuminator is uncertain, although the simplest explanation would be that the pair constitutes a widely separated binary.

Although HST has well established the optical and near-infrared morphology of RAFGL 2688 (Sahai et al. 1998a,b), a detailed understanding of the nebula remains elusive. The kinematics of its molecular emission are particularly puzzling (see Cox et al. 2000, Kastner et al. 2001, and references therein). This emission seems to trace multipolar, radially directed outflows, some with no counterparts at optical or infrared wavelengths; alternatively, the emission may be interpreted in terms of a combination of radial and azimuthal velocity fields. Deepening the mystery of the structure of RAFGL 2688 are recent mid-infrared and radio imaging observations of dust emission that appear to trace highly collimated (and perhaps precessing) outflows (Morris & Sahai 2000; Jura et al. 2000).

Polarimetric imaging observations remain central to an understanding of the structure and evolution of RAFGL 2688. While the nebula is well characterized polarimetrically in the optical and near-infrared, little or no spatially resolved polarimetric imaging data exists

for wavelengths $> 2\mu\text{m}$. Here, we report on infrared polarimetric imaging of RAFGL 2688 at $4.5\mu\text{m}$ with the Infrared Space Observatory (ISO, Kessler et al. 1996). In conjunction with previous HST near-infrared polarimetric imaging and ground-based direct mid-infrared imaging, the ISO polarimetric imaging yields insights into the relative contributions of direct and unpolarized starlight and of the grain size distribution in RAFGL 2688.

2. Observations

Data presented here were obtained with the ISO direct imaging instrument, ISOCAM (Cesarsky et al., 1996), using its long wavelength (LW) camera and passband filter LW1. The detector format was 32×32 pixels. The response of LW1 is centered at $4.5\mu\text{m}$ and is relatively flat, extending from 4 to $5\mu\text{m}$.

ISOCAM was equipped with polarizers oriented at 0, 120, and 240 degrees. Polarimetric imaging was set up according to the standard observing template CAM05 (Siebenmorgen 1996). The corresponding ISO observation numbers, TDT, are: 76800602, 76800703, 76800804, 76800905, 76801006, 76801107, 76801208, 76801309, 76801410 and 76801511. We used a 4×4 raster with a raster step size of $6''$, the $1.5''$ lens, a readout time for each exposure of 2.1 s, and a gain of one. Initially, we took 155 exposures on the source to stabilize the detector and then a raster through the free “hole” of the entrance wheel. At each raster position 26 exposures were read out. This procedure was carried out for each of the three polarizers. The polarizer rasters were repeated in three observing cycles.

3. Results

3.1. Processed ISOCAM LW1 images

The data were reduced with the ISOCAM interactive analysis system (CIA version 4.0, Ott et al. 1996). Only basic reduction steps, such as dark current subtraction, removal of cosmic ray hits and transient correction, are applied to the data. These steps are described together with calibration uncertainties in Blommaert et al. (2001). The coadded images at each raster position were projected on the sky to derive the final mosaics. The mosaics have a $66'' \times 68''$ total field of view and a pixel scale of $1.5''$. The polarized signal is found to be consistent between the individual observing cycles. The average of all cycles gives the final mosaic image for each polarizer. The output of this image processing procedure therefore consisted of four images, each of total integration time 1124 s: three polarized images (one for each of the three polarization filters) and one “unpolarized” or total intensity image (obtained through the “hole” position).

As part of the ISO calibration program, the zodiacal light and a set of (unpolarised) photometric standard stars was observed by repeating CAM05 observing templates. From those calibration measurements an instrumental polarization of $<1.5\%$ is derived (Siebenmorgen 1999). This instrumental polarization is small enough to have negligible effect on the results described in this paper.

The total intensity image of RAFGL 2688 is displayed in Fig. 2, alongside a 3420 s ISOCAM LW1 image of the infrared-bright standard star HIC 85317 (spectral type A4V, $V=6.5$ mag, TDT=35600401). The comparison emphasizes the rather complex, asymmetric point spread function (PSF) of ISOCAM at $4.5\mu\text{m}$. The six-pointed structure of the PSF is due to the support structure for the secondary mirror of the telescope. Although this point spread function dominates the structure of both the RAFGL 2688 and standard star

images, it is also apparent that RAFGL 2688 is extended relative to the standard. This is seen most clearly in the comparisons of nonlinear greyscale images (Fig. 2, bottom panels) and plots of intensity vs. radius for RAFGL 2688 and the standard star (Fig. 3), the latter of which reveals twice as much or more light in the RAFGL 2688 images as in the PSF at distances $\sim 10''$ from the bright central PSF core.

3.2. ISOCAM 4.5 μm polarimetric map

The polarimetric image set obtained with the three polarizing filters in the LW camera is sufficient to uniquely determine the Stokes parameters for each image pixel (x, y) . Specifically, we find $I(x, y), Q(x, y), U(x, y)$ from the image set $P_0(x, y), P_{120}(x, y), P_{240}(x, y)$ as follows:

$$I(x, y) = \frac{2}{3}[P_0(x, y) + P_{120}(x, y) + P_{240}(x, y)] \quad (1)$$

$$Q(x, y) = \frac{2}{3}[2P_0(x, y) - P_{120}(x, y) - P_{240}(x, y)] \quad (2)$$

$$U(x, y) = -\frac{2}{\sqrt{3}}P_{120}(x, y) + \frac{2}{\sqrt{3}}P_{240}(x, y) \quad (3)$$

The degree p and position angle θ of linear polarization may then be derived from the Stokes parameters in the usual manner, i.e.,

$$p(x, y) = \frac{(Q^2(x, y) + U^2(x, y))^{1/2}}{I(x, y)} \quad (4)$$

and

$$\theta(x, y) = \frac{1}{2} \tan^{-1} \frac{U(x, y)}{Q(x, y)}. \quad (5)$$

Polarization maps so obtained from ISOCAM polarimetric imaging have been presented for the Crab nebula (Tuffs et al. 1999), the protostellar system HH 108MMS (Siebenmorgen & Krügel 2001), the starburst NGC 1808 galaxy (Siebenmorgen et al., 2001), and a sample of ultraluminous galaxies (Siebenmorgen & Efstathiou 2001).

The ISO polarization map obtained for RAFGL 2688 (Fig. 4) shows hints of centrosymmetry, particularly in its northern regions. The center of symmetry of this portion of the polarimetric map appears to lie near the bright central region of the image. This spatial polarization structure suggests that much of the northern region of the ISO $4.5 \mu\text{m}$ image of RAFGL 2688 is, in fact, scattered light, and that the source of illumination lies in the vicinity of the image intensity peak. However, the structure of the ISO polarimetric map is, overall, much less well organized than that of the HST/NICMOS polarization map (Fig. 1). In particular, the relative contributions from nebulosity and PSF are not clear from Fig. 1; nor is it obvious whether any extended $4.5 \mu\text{m}$ emission is dominated by scattering (as is undoubtedly the case at $2 \mu\text{m}$) or by direct, thermal emission. Evidently, either the ISO polarimetric map suffers from systematic distortions, or there are significant differences in the spatial distribution and degree of polarization in RAFGL 2688 between $2 \mu\text{m}$ and $4.5 \mu\text{m}$.

4. Reconstruction of Direct and Polarimetric Images

To investigate the extent to which the prominent signature of the PSF in the individual polarimetric images affects the ISO $4.5 \mu\text{m}$ polarimetric map, we attempted to remove the PSF signature from these images and that of the total intensity image. To this end we have employed two popular deconvolution methods, maximum likelihood (hereafter ML; Richardson 1972; Lucy 1974) and maximum entropy (e.g., Hollis, Dorband, & Yusef-Zadeh 1992; hereafter ME), using programs that are part of the standard IDL Astronomy Library⁵.

Both ML and ME techniques require a deconvolution “kernel” consisting of the best known representation of the instrumental PSF. One then makes an initial estimate of the

⁵<http://idlastro.gsfc.nasa.gov/>

“true” source intensity distribution, i.e., the source intensity distribution that would be detected in the absence of instrumental broadening. This image is convolved with the PSF and is then compared with the observed image intensity distribution. The resulting difference image (or “residual image”) is stored for reference. The “true” image intensity distribution is then modified accordingly (following either the ML or ME algorithm prescription), and the process is repeated. The change in residual image statistics (e.g., residual image maximum and standard deviation) over successive iterations of either the ML or ME schemes can be used to assess the progress of image deconvolution.

4.1. Reconstructed ISOCAM 4.5 μ m total intensity image

The results of iterative deconvolutions of the ISOCAM LW1 total intensity image using ML and ME methods are displayed in Figs. 5 and 6. For these deconvolutions, we adopted as the instrumental PSF the ISOCAM LW1 image of HIC 85317. It is apparent from both figures that the ML and ME methods produce very similar results and, furthermore, that the two methods asymptotically approach their “best guesses” for the “true” image at similar rates. Specifically, after ~ 15 iterations, the net changes in both the maximum and the standard deviation of the residual image (from their original values) approach $\sim 90\%$ of the differences between their original and asymptotic values (Fig. 5). We find that, for either the ML or ME methods, iterating more than about 20 times introduces image artifacts, such as negative values and spurious off-source features.

Notably, *both the ML and ME deconvolution methods produce the same fundamental result for the reconstructed total intensity image* (Fig. 6). This reconstructed image consists of a compact, bright central source, representing $\sim 90\%$ of the total source intensity, surrounded by fainter nebulosity. Most of the nebulosity lies to the north-northeast of the bright, compact source. This source structure is consistent with the morphology of the

polarimetric map (§3.2), i.e., the bright, central source appears to illuminate a region of reflection nebulosity to its north-northeast.

4.2. Reconstructed ISOCAM polarization map

We applied the ML method to the individual LW1 polarimetric images, to obtain a deconvolved polarization image set $P'_0(x, y), P'_{120}(x, y), P'_{240}(x, y)$. For these deconvolutions, we again adopted the ISOCAM LW1 image of HIC 85317 as representative of the instrumental PSF, under the assumption that the polarizing filters produce negligible additional point source distortions. To obtain each polarimetric image, we performed 16 iterations of the ML algorithm. The resulting deconvolved LW1 polarimetric images of RAFGL 2688 (not shown) are qualitatively similar to the deconvolved total intensity image described in the preceding section, i.e., a compact central source with nebulosity extending to the north-northeast.

The polarization map constructed from the images $P'_0(x, y), P'_{120}(x, y), P'_{240}(x, y)$ (hereafter referred to as the reconstructed polarization map) is presented in Fig. 7. The centrosymmetry evident in the northern regions of the “raw” polarimetric map (Fig. 4) is more pronounced in this reconstructed polarization map. Like the “raw” map, the reconstructed map also displays a minimum of polarization near the intensity peak in the total intensity image, and a somewhat disorganized polarization pattern to the south of the intensity peak.

5. Discussion

5.1. Can the results of the deconvolutions be trusted?

It is well known that the results of either ML or ME deconvolution are not necessarily unique. Indeed, depending on the quality of both data and PSF model, the results of either technique can be spurious. Furthermore, we are not aware of a rigorous proof that demonstrates that deconvolution of polarimetric images preserves polarization information. Nonetheless, there are several reasons to conclude that the deconvolution results just described are valid.

First, we find strong consistency between the results of the ML and ME methods. The two methods converge to essentially the same end results (Figs. 5,6). Second, the reconstructed ISOCAM 4.5 μm image and polarization map of RAFGL 2688 are qualitatively consistent with the results of previous near-infrared imaging polarimetry and direct mid-infrared imaging. Specifically, in the reconstructed ISOCAM image, RAFGL 2688 is extended along a position angle $\sim 15^\circ$, a result also obtained from high-resolution 2 μm and 9 μm imaging (Weintraub et al. 2000; Morris & Sahai 2000) but that can be only marginally inferred from the raw ISO images (e.g., Fig. 4).

Third, the reconstructed polarization map (Fig. 7) represents an improvement over the polarization map constructed from “raw” images (Fig. 4). In particular, note the stronger centrosymmetry and larger values of polarization in the northern regions of the map in Fig. 7. Both improvements would be expected from a successful deconvolution procedure; such a procedure should correct for instrumental stray light at low spatial frequencies, thereby removing “contaminating” flux that would otherwise suppress the degree of polarization, especially in regions of low source surface brightness.

We conclude that the reconstructed ISOCAM 4.5 μm total intensity image and

polarization map of RAFGL 2688 are trustworthy.

5.2. The nature of the 4.5 μm emission from RAFGL 2688

The ISOCAM polarimetric map of RAFGL 2688 reveals that the extended nebulosity to the north-northeast is highly polarized, indicative of reflection nebulosity. The centrosymmetry of this polarization pattern about the 4.5 μm intensity peak indicates that the intensity peak is the likely source of illumination of the nebulosity. This source is very likely a combination of direct photospheric emission from the central F-type supergiant (e.g., Cohen & Kuhi 1977) and photospheric emission reprocessed by dust grains at characteristic temperatures of $\gtrsim 140$ K (Persi et al. 1999).

The apparent “emergence” of the central source at longer infrared wavelengths is seen in Fig. 8. The source is only seen via reflection at 2 μm (lefthand panel; see also Weintraub et al. 2000) whereas, evidently, it makes a substantial contribution to the nebular morphology (in the form of a strong point-like source and diluted polarization) near the center of the nebula at 4.5 and 8.8 μm (central and righthand panels). Similar behavior is observed in infrared reflection nebulosity surrounding young stellar objects, and is usually interpreted as a decrease in scattering opacity with increasing wavelength (e.g., Fischer 1995). We caution, however, that the registration of the three images in Fig. 8 is not certain to better than $\sim 1''$, the ISOCAM polarization imaging suffers from relatively low spatial resolution, and there is no polarization information in the 8.8 μm image. Furthermore, there are multiple sources of 2 μm photons in RAFGL 2688 (Weintraub et al. 2000). Hence it may be somewhat premature to conclude that the same source that illuminates the nebula at 2 μm also illuminates reflection nebulosity at 4.5 and 8.8 μm .

While it appears we have detected the central illuminating source at 4.5 μm , this

source evidently is highly obscured along our line of sight. This conclusion follows from the ratio of nebular surface brightness to point source intensity; specifically, at an angular displacement of $6''$ along the polar axis of the nebula from the central point source, we find that the surface brightness of scattered light is $\sim 1\%$ of the integrated intensity of the central source. For a reflection nebula whose dust density is inversely proportional to the square of the angle from the source of illumination (θ), the scattering optical depth (τ_s) is related to the ratio of scattered to incident starlight, $I_s(\theta)/I_0$, via

$$\tau_s(\theta) = 8\pi \frac{I_s(\theta)}{I_0} \frac{\theta^2}{\Delta\phi} \quad (6)$$

where $\Delta\phi$ is the solid angle subtended by a pixel (Jura & Jacoby 1976; Kastner 1990). Assuming the integrated intensity of the central source as measured in our images accurately represents the available illuminating flux, I_0 , then the measured ratio $I_s(6'')/I_0 \approx 0.01$ would suggest a scattering optical depth $\tau_s(6'') \approx 4$. This result is seemingly at odds with our detection of very high levels of polarization ($\sim 60\%$) in this region, however; such a high degree of polarization requires that single scattering is dominant over multiple scattering. We conclude that, along our line of sight, the central object is highly attenuated at $4.5 \mu\text{m}$, such that the measured value of $I_s(6'')/I_0$ is an overestimate. A conservative lower limit to the degree of $4.5 \mu\text{m}$ extinction toward the central source is provided by the requirement that $\tau_s < 1$, suggesting $A_{4.5\mu\text{m}} > 1.5$.

Fig. 9 shows a comparison of percent polarization vs. radius from the central star, for the $2 \mu\text{m}$ (HST/NICMOS) and $4.5 \mu\text{m}$ (ISOCAM) polarimetric imaging observations. The figure demonstrates that percent polarization is more or less independent of wavelength within the nebula, between $\sim 2 \mu\text{m}$ and $5 \mu\text{m}$, at radial offsets well displaced from the star. This behavior is similar to that observed in the evolved bipolar reflection nebula OH 231.8+4.2 (Shure et al. 1995), although the OH 231.8+4.2 observations only extended to $3.6 \mu\text{m}$. From the large values of polarization in RAFGL 2688 at both $2 \mu\text{m}$ and

4.5 μm , we may safely conclude that scattering dominates the nebular emission at these wavelengths; i.e., there is little or no contribution from thermal emission from the dust grains in RAFGL 2688, even at wavelengths as long as $\sim 5 \mu\text{m}$. As no polarization data have been obtained for this nebula at longer wavelengths we are, as yet, unable to ascertain the nature of the lobe emission seen at 8.8 μm (Fig. 8).

5.3. Dust grain size distribution

Most detailed modeling of reflection nebulae at $\sim 5 \mu\text{m}$ performed thus far has been geared toward interpreting large-aperture polarization measurements (e.g., Heckert & Smith 1988; Pendleton et al. 1990; Fischer 1995; Shure et al. 1995) rather than spatially resolved polarization imaging. Nevertheless, based on the wavelength independence of polarization of RAFGL 2688 and the typical polarization values of $\sim 60\%$ at large offsets from the central star, we conclude that the bulk of the dust grains in the RAFGL 2688 reflection nebula are significantly smaller than the wavelengths employed in the HST/NICMOS and ISOCAM imaging studies. That is, the grains have typical radii $a < 1 \mu\text{m}$. This result, which is similar to that obtained by Shure et al. (1995) for OH 231.8+4.2, follows from the straightforward analytical treatment of light scattering by small particles (van de Hulst 1957) as well as from the more detailed, but limited, modeling of dust grain populations in infrared reflection nebulae performed to date (Pendleton et al. 1990; Fischer 1995).

6. Summary

We have obtained 4.5 μm polarimetric images of the evolved bipolar reflection nebula RAFGL 2688 with the CAM mid-infrared camera aboard the Infrared Space Observatory. The observations are strongly affected by the complex CAM point spread function. The

source structure in reconstructed (deconvolved) images is that of a bright central object with faint nebulosity extending to the north-northeast. The position angle of extended nebulosity is the same as that seen in ground-based near-infrared images obtained at other wavelengths. A polarization map constructed from deconvolved, polarized images displays a large degree of polarization and a centrosymmetric pattern of position angle within the faint, extended nebulosity, while the bright central source displays much lower levels of polarization and disorganized patterns of polarization position angle.

The pattern and degree of polarization within the extended nebulosity, as revealed in the reconstructed image and polarization map, confirms that scattering is the dominant source of nebular light. Comparison with previous space-based (HST/NICMOS) polarimetric imaging indicates that the degree of polarization within the extended RAFGL 2688 nebula is independent of wavelength, suggesting that small ($< 1 \mu\text{m}$) grains do most of the scattering of starlight.

Further, detailed modeling is required to provide additional insight into the circumstellar structure and grain properties of evolved, bipolar nebulae such as RAFGL 2688. It would also be of great value to obtain mid-infrared imaging polarimetry of RAFGL 2688 at higher resolution, to ascertain the precise location of the illuminating source at $\sim 5 \mu\text{m}$. as well as at longer wavelengths, to determine whether scattering is still important or even dominant beyond $5 \mu\text{m}$.

The authors thank Mark Morris and Raghvendra Sahai for the use of their $8.8 \mu\text{m}$ Keck image of RAFGL 2688. CIA is a joint development by the ESA Astrophysics Division and the ISOCAM Consortium. The ISOCAM Consortium is led by the ISOCAM PI, C. Cesarsky. ISO research by JHK and JL was supported by JPL grants 1230950 and 1211136 to RIT.

REFERENCES

Blommaert J., Siebenmorgen R., Coulais A., et al., 2001, “ISO Handbook Volume III (CAM)”, SAI-99-057/Dc, Version 1.2, <http://www.iso.vilspa.esa.es>

Cesarsky C., Abergel A., Agnèse P. et al., 1996, *A&A* 315, L32

Cohen, M., & Kuhi, L.V. 1977, *ApJ*, 213, 79

Cox, P., Lucas, R., Huggins, P.J., Forveille, T., Bachiller, R., Guilloteau, S., Mallard, J.P., & Omont, A. 2000, *A&A*, 353, L25

Fischer, O. 1995, *RMA*, 8, 103

Heckert, P.A., & Smith, P.S. 1998, *AJ*, 95, 873

Hollis, J. M., Dorband, J. E., & Yusef-Zadeh, F. 1992, *ApJ*, 386, 293

Jones, T.J., & Dyck, H.M. 1978, *ApJ*, 220, 159

Jura, M., & Jacoby, G. 1976, *Ap Letters*, 18, 5

Jura, M., Turner, J.L., Van Dyk, S., & Knapp, G. 2000, *ApJ*, 528, L105

Kastner, J.H. 1990, Ph.D. thesis, UCLA

Kastner, J.H., & Weintraub, D.A. 1995, *AJ*, 109, 1211

Kastner, J.H., Soker, N., & Rappaport, S., eds. 2000a, “Asymmetrical Planetary Nebulae II: From Origins to Microstructures”, *ASP Conf. Ser.* Vol. 199

Kastner, J.H., Weintraub, D.A., Gately, I., & Henn, L. 2001, *ApJ*, 546, 279

Kessler M.F., Steinz J.A., Andregg M.E., et al., 1996, *A&A* 315, L27

Lucy, L. B. 1974, *AJ*, 79, 745

Morris, M., & Sahai, R. 2000, in “Asymmetrical Planetary Nebulae II: From Origins to Microstructures,” eds. J.H. Kastner, N. Soker, & S. Rappaport, *ASP Conf. Ser.* Vol. 199, p. 143

Ney, E.P., Merrill, K.M., Becklin, E.E., Neugebauer, G., & Wynn-Williams, C.G. 1975, ApJ, 198, L129

Ott S., Abergel A., Altieri B., et al., 1996, ASAP Conference series, Vol. 125, 1997

Pendleton, Y., Tielens, A.G.G.M., & Werner, M. 1990, ApJ, 349, 107

Persi, P., Cesarsky, D., Marenzi, A.R., Preite-Martinez, A., Rouan, D., Siebenmorgen, R., Lacombe, F., Tiphene, D. 1999, A&A, 351, 201

Richardson, W. H. 1972, OSAJ, 62, 55

Sahai, R., Hines, D., Kastner, J.H., Weintraub, D.A., Trauger, J. T., Rieke, M. J., Thompson, R. I., Schneider, G. 1998a, ApJ, 492, L163

Sahai, R. et al. 1998b, ApJ, 493, 301

Shure, M., Sellgren, K., Jones, T. J., & Klebe, D. 1995, AJ, 109, 721

Siebenmorgen R., 1996, “Polarimetric imaging with ISOCAM: C05 Observer’s Manual”, ESA/SAI/96-238/Dc, <http://www.iso.vilspa.esa.es>

Siebenmorgen, R. 1999, “ISO Polarisation Observations,” R.J. Laureijs and R. Siebenmorgen, ESA-SP435, ISBN 92-9092-740-2, <http://www.iso.vilspa.esa.es>

Siebenmorgen, R., Krügel, E., 2001, A&A 364, 625

Siebenmorgen, R., Krügel, E., & Laureijs, R.J. 2001, A&A 377, 735

Siebenmorgen, R., & Efstathiou, A. 2001, A&A 376, L35

Tuffs, R.J., Siebenmorgen, R., & Gallant, Y.A. 1999, “Mid-infrared polarimetric mapping of the Crab Nebula,” in: Observing Polarisation with the Infrared Space Observatory, Eds.: R.J. Lauriejs & R. Siebenmorgen, ESA-SPC, available at <http://www.iso.vilspa.esa.es/meetings/polarisation/paper/web/>

van de Hulst, H.C. 1957, “Scattering of Light by Small Particles” (San Francisco: Wiley), p. 63

Weintraub, D.A., Kastner, J.H., Sahai, R., & Hines, D. 2000, ApJ, 531, 401

Zuckerman, B., Gilra, D. P., Turner, B. E., Morris, M., & Palmer, P. 1976, ApJ, 205, L15

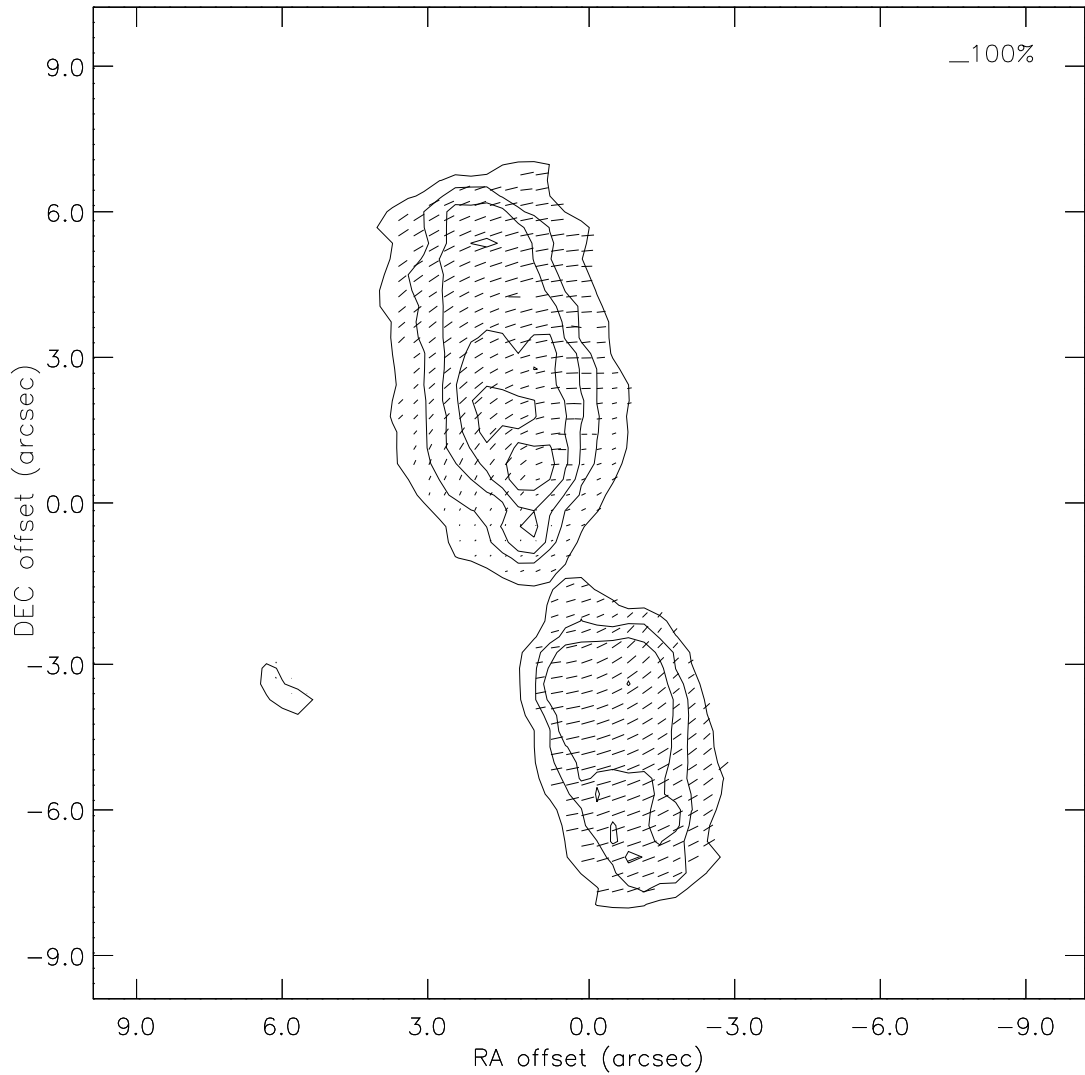


Fig. 1.— Hubble Space Telescope near-infrared ($2 \mu\text{m}$) image (contours) and polarimetric map obtained with the Near-Infrared Camera and Multi-Object Spectrometer (NICMOS), constructed from archival images. Vectors indicate the degree and position angle of polarization at each position across the image. See also Sahai et al. (1998a) and Weintraub et al. (2000).

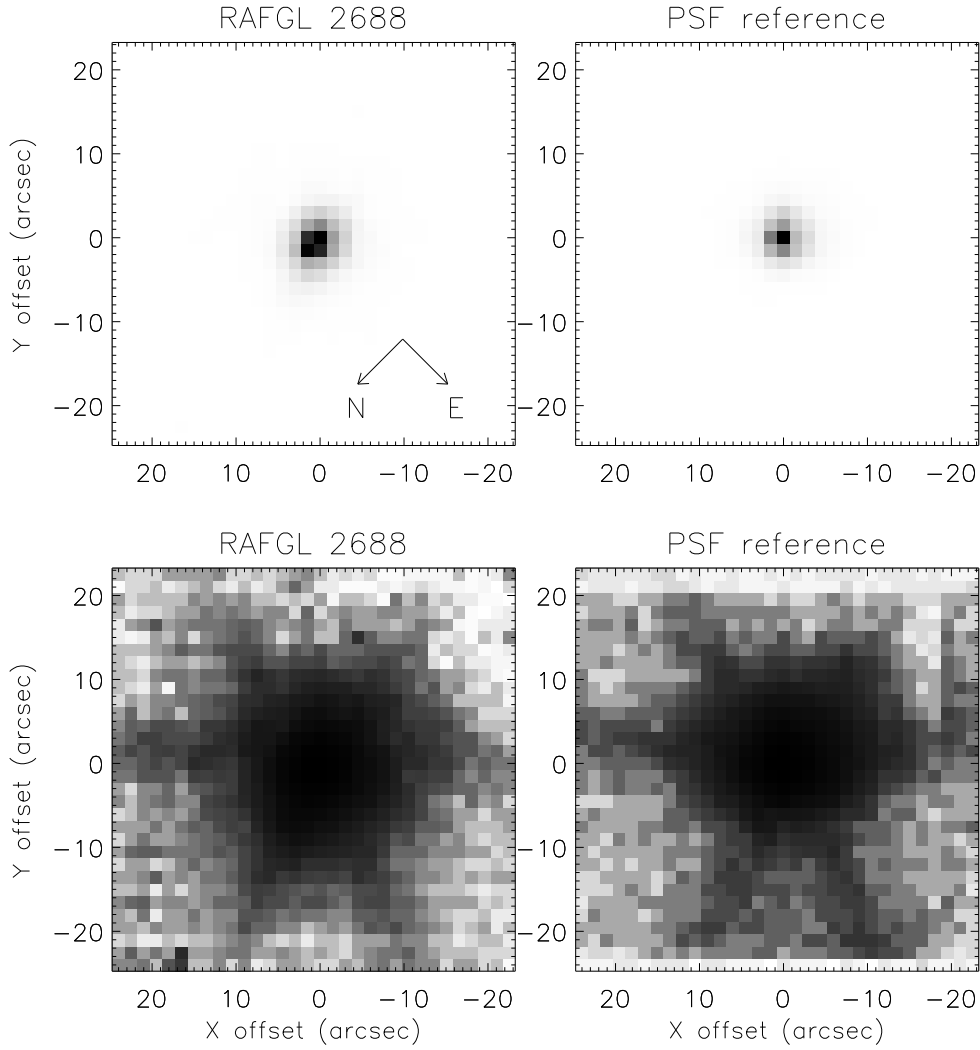


Fig. 2.— ISOCAM LW1 ($4.5 \mu\text{m}$) total intensity images of RAFGL 2688 (left panels) and the standard star HIC 85317 (right panels). Images at top are displayed with a linear greyscale representation, while images at bottom are displayed with a nonlinear greyscale emphasizing low-level structure in the ISOCAM LW1 point spread function. Images are displayed in the orientation in which they were obtained by the detector, i.e., with image rows and columns representing detector rows and columns, respectively.

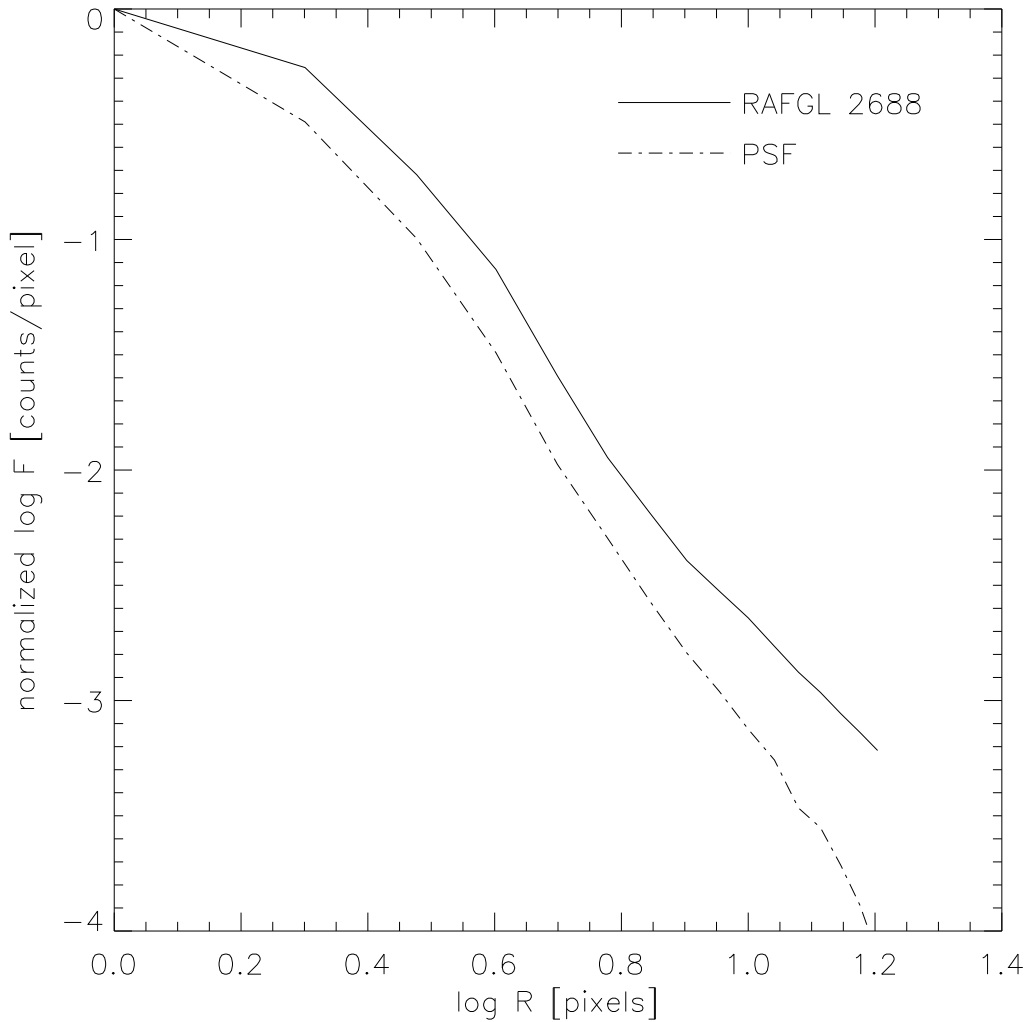


Fig. 3.— Profiles of intensity vs. radius for RAFGL 2688 (solid curve) and standard star (dashed curve). Both curves are normalized to their peak intensities.

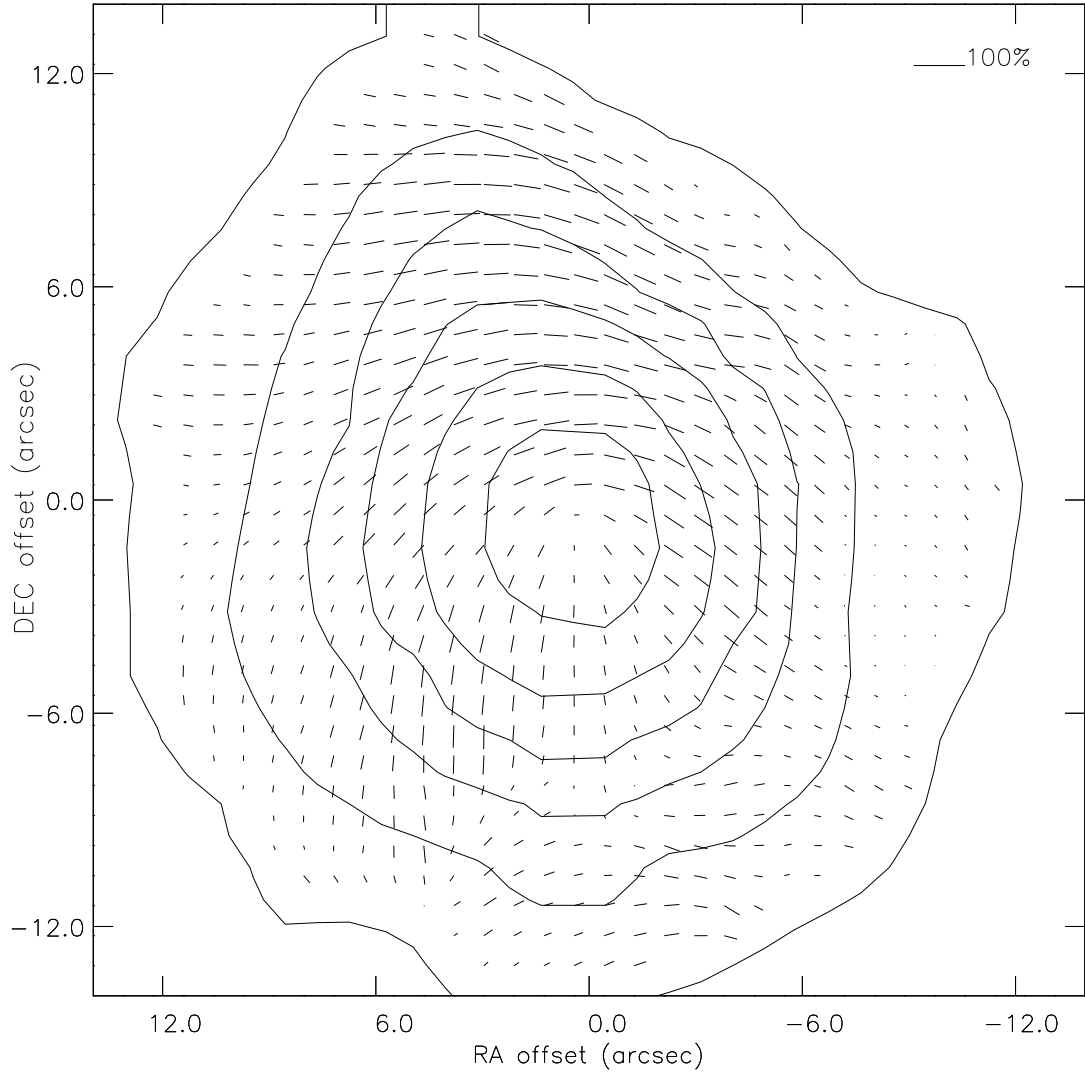


Fig. 4.— Polarization map of RAFGL 2688 constructed from processed LW1 images obtained through the three polarizing filters in the LW camera. The orientation and length of each vector indicates the direction and relative degree of linear polarization, respectively, for a given pixel. Vectors are displayed for pixels in which the surface brightness is at least 10 times the pixel-to-pixel noise level in the individual polarized images. The map is overlaid on a contour plot of the total intensity image of Fig. 2. Map and image have been rotated to the celestial coordinate reference frame. Contours are displayed at intervals of 0.4 dex, with the lowest contour at 10 times the noise level in the individual polarized images.

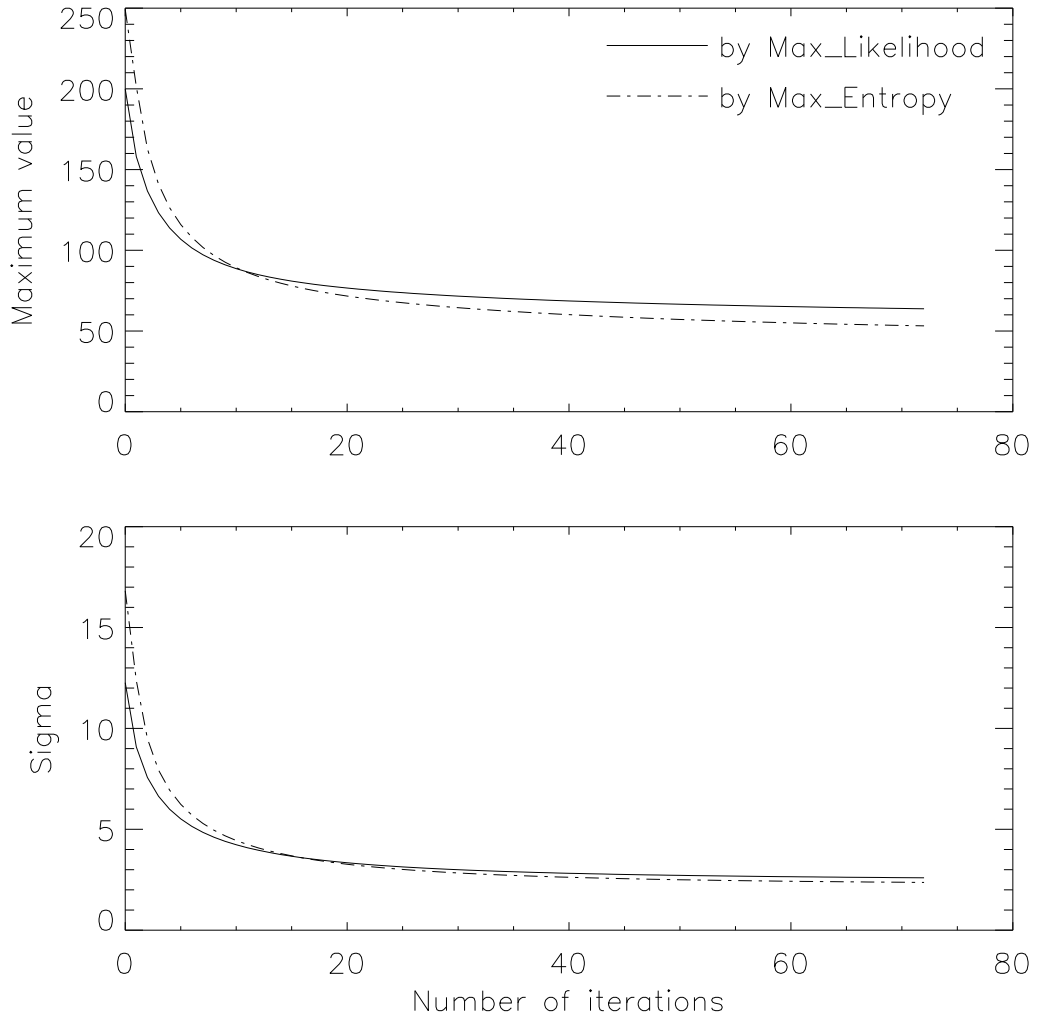


Fig. 5.— Plot of the maximum value and standard deviation of the residual image — i.e., the difference between the observed intensity distribution and the inferred, “true” intensity distribution convolved with instrumental PSF — as a function of iteration number. Results for maximum likelihood and maximum entropy deconvolution techniques are shown as solid and dashed curves, respectively.

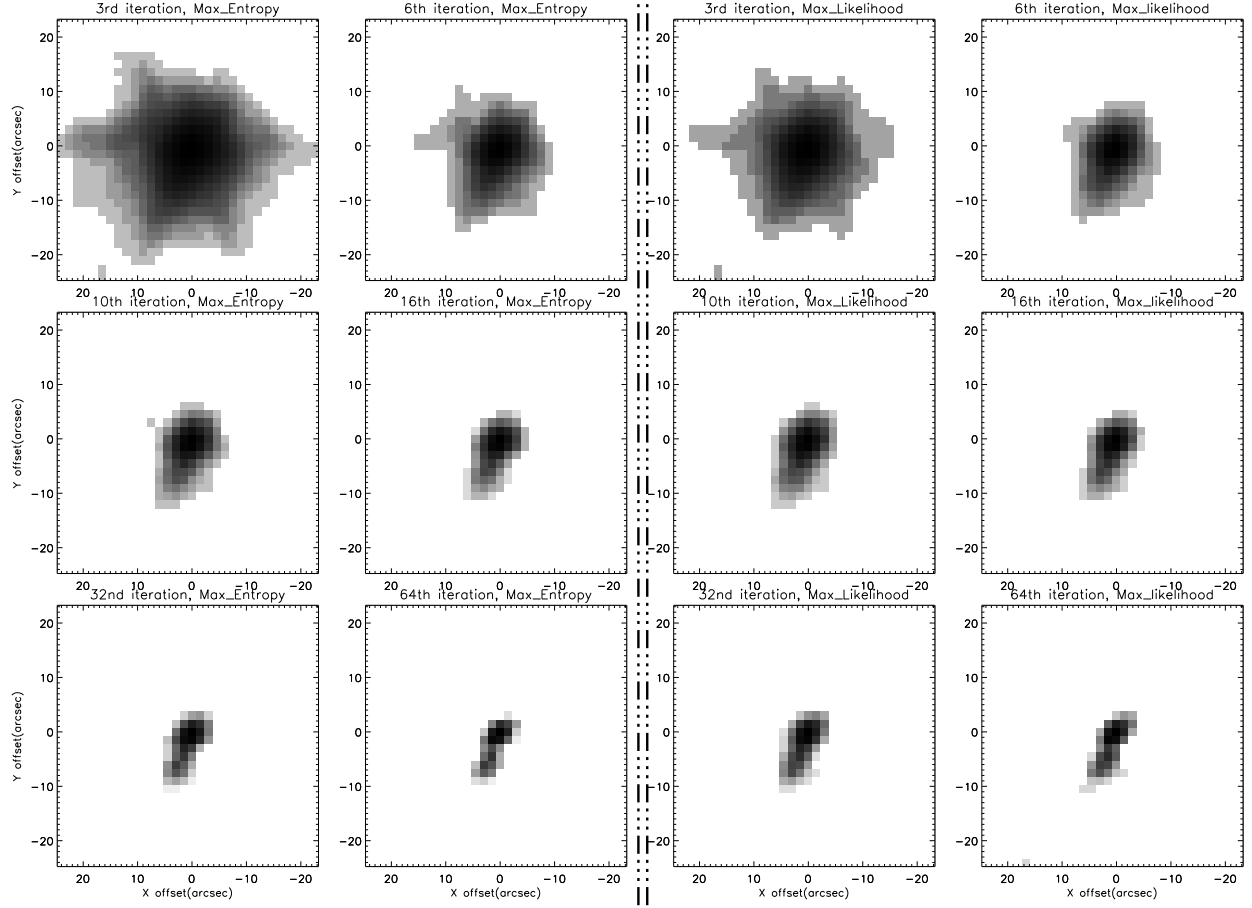


Fig. 6.— Reconstructed total intensity ISOCAM 4.5 μ m images of RAFGL 2688 inferred from the ML (right panels) and ME (left panels) techniques. The number of iterations performed to obtain each reconstructed image increases from upper left to lower right, as indicated in each panel.

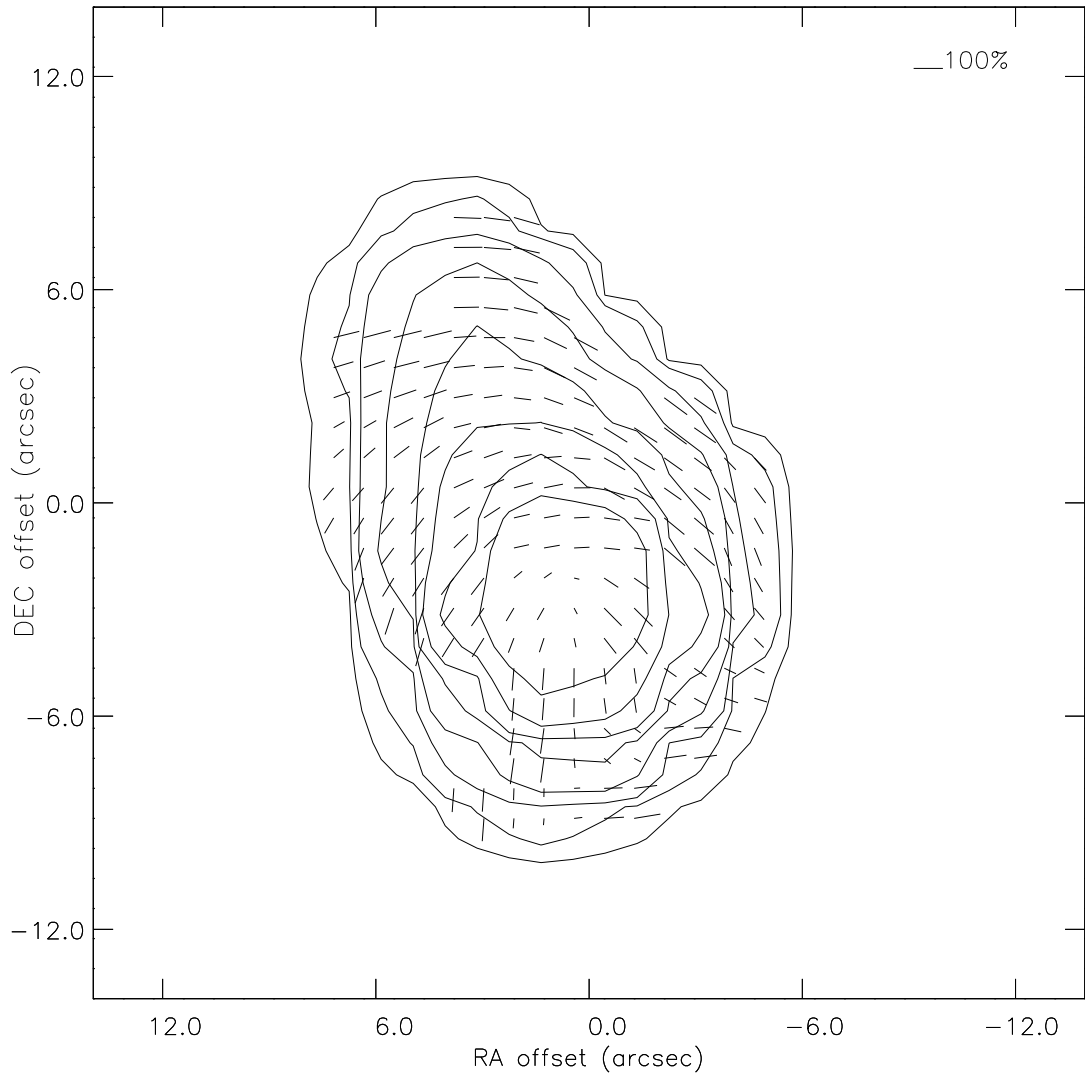


Fig. 7.— Polarization map of RAFGL 2688 constructed from deconvolved LW1 polarimetric images, overlaid on a contour plot of the reconstructed total intensity image. This reconstruction is the result of 16 iterations of the maximum likelihood method. Polarization vectors are displayed for pixels in which the surface brightness is at least 5 times the pixel-to-pixel noise level in the individual polarized images. Contours are displayed at intervals of 0.4 dex, with the lowest contour at 5 times the noise level in the individual polarized images.

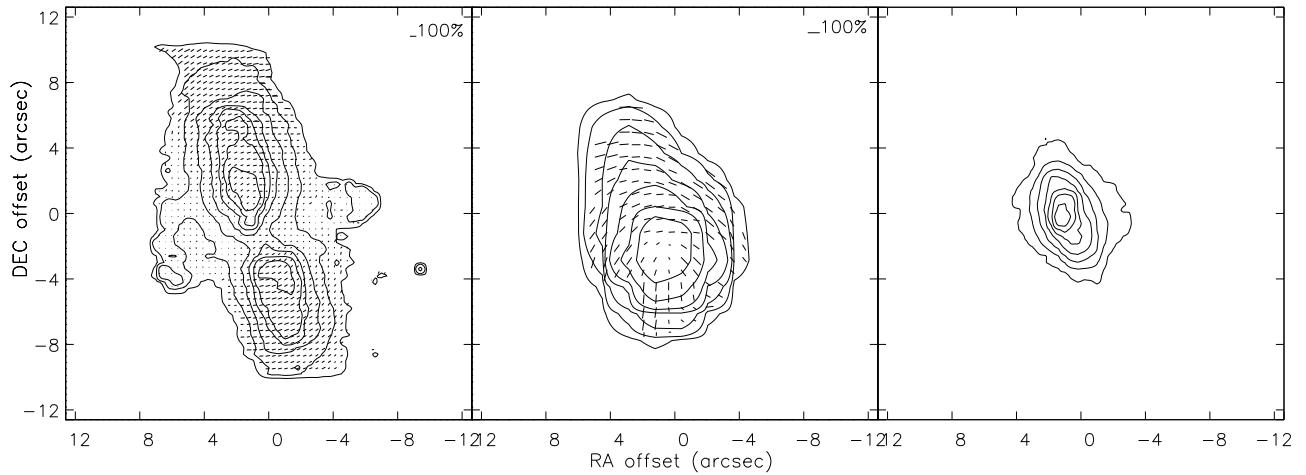


Fig. 8.— Near-infrared polarimetric images of RAFGL 2688 obtained at $2 \mu\text{m}$ with HST/NICMOS (left) and at $4.5 \mu\text{m}$ with ISOCAM (center), and a direct $8.8 \mu\text{m}$ image obtained with the 10 m Keck telescope and MIRLIN mid-infrared camera (right; from Morris & Sahai 2000).

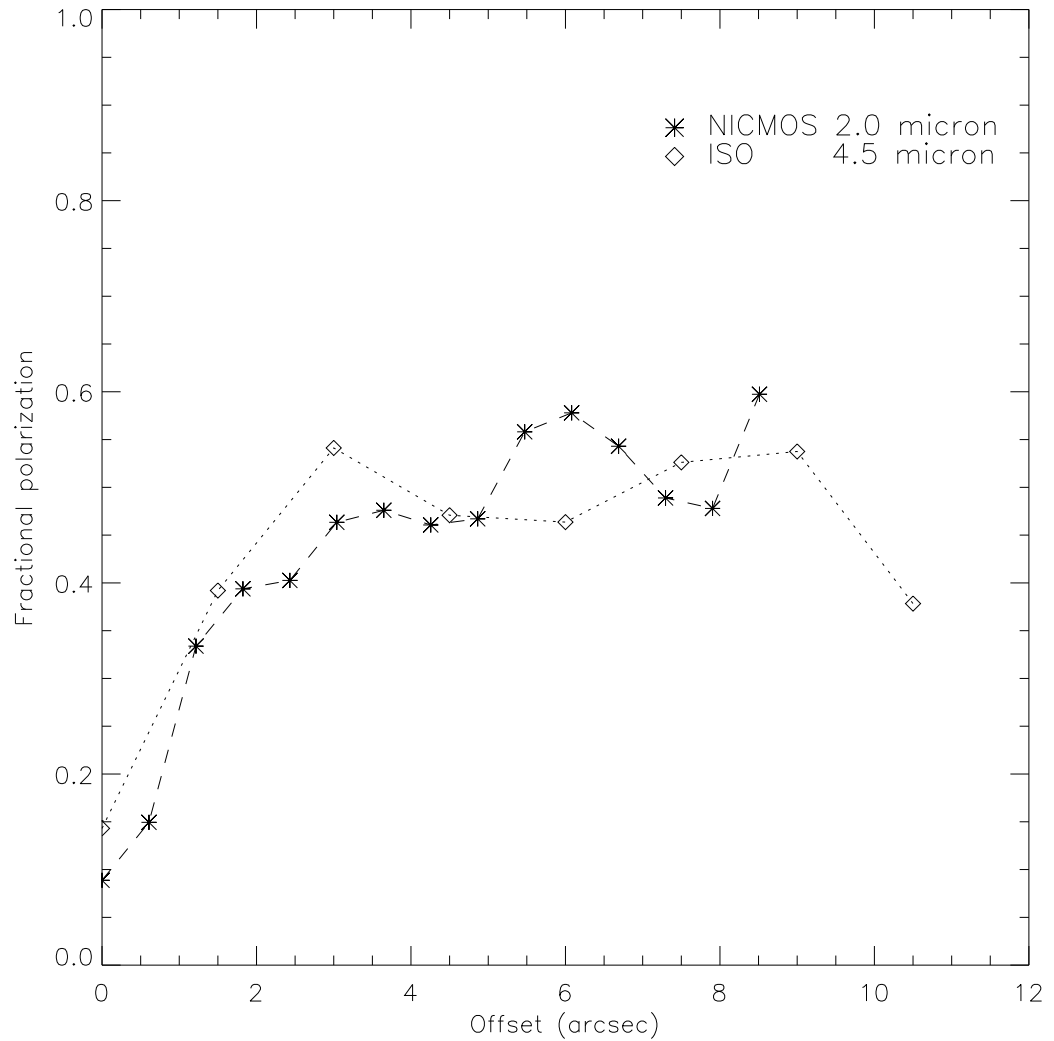


Fig. 9.— Plot of percent polarization vs. distance from the central star, obtained from linear cuts along the polar axis of RAFGL 2688 in the $2 \mu\text{m}$ HST/NICMOS and $4.5 \mu\text{m}$ ISOCAM images.